Evaluating the Beamforming Impact on Channel Dispersion Characterization Using Multiscenario Sub-THz Channel Measurements

Peize Zhang, *Member, IEEE*, Mar Francis de Guzman, *Member, IEEE*, Yejian Lyu, Katsuyuki Haneda, *Member, IEEE*, Nuutti Tervo, *Member, IEEE*, Aarno Pärssinen, *Senior Member, IEEE*, and Pekka Kyösti

***Abstract*— To provide substantially high capacity, future 6G networks will be able to operate in higher frequency bands than current 5G networks. However, owing to the significant differences in channel characteristics between lower bands (<100 GHz) and subterahertz (sub-THz) band (i.e., 100–300 GHz), novel waveform and air interface design for sub-THz systems need to account for the radio channels observed by practical beam patterns. In this article, we investigate the beamforming impact on the characterization of angular and time dispersion based on extensive measured channel data at 142 GHz across multiple scenarios. A postprocessing method for analysis of beamforming impact on channel dispersion is proposed using measured propagation channel data. Since sub-THz radio links necessitate high antenna gains, we first find the potential beam directions from beamformed channels and then form single-beam and multibeam patterns toward desired directions under practical constraints. The angular spread of the beamformed channels observed by steered beams will be widened especially in line-of-sight scenarios. The beam-weighted radio channel is considered the basis of calculating time dispersion parameters, i.e., beam gains are multiplied by the measured propagation path gains before the analysis. Preliminary results show that the reduction of delay spread and maximum excess delay depends mainly on scenario, link distance, and used beamwidth, and partly on sidelobe level.**

Received 5 February 2024; revised 3 October 2024; accepted 28 October 2024. Date of publication 7 November 2024; date of current version 17 January 2025. This work was supported in part by the Hexa-X-II Project through the Smart Networks and Services Joint Undertaking (SNS JU), European Union's Horizon Europe Research and Innovation Programme, under Grant 101095759; in part by the Research Council of Finland (former Academy of Finland) Multipath Project under Grant 348980; and in part by the 6G Flagship Programme under Grant 346208. *(Corresponding author: Peize Zhang.)*

Peize Zhang, Nuutti Tervo, and Aarno Pärssinen are with the Centre for Wireless Communications, University of Oulu, 90570 Oulu, Finland (e-mail: peize.zhang@oulu.fi; nuutti.tervo@oulu.fi; aarno.parssinen@oulu.fi).

Mar Francis de Guzman and Katsuyuki Haneda are with the Department of Electronics and Nanoengineering, Aalto University School of Electrical Engineering, 02150 Espoo, Finland (e-mail: francis.deguzman@aalto.fi; katsuyuki.haneda@aalto.fi).

Yejian Lyu was with the Antenna, Propagation and Millimeter-Wave Systems Section, Department of Electronic Systems, Faculty of Engineering and Science, Aalborg University, 9220 Aalborg, Denmark. He is now with the Terahertz Wireless Communication Laboratory, Shanghai Jiao Tong University, Shanghai 200240, China (e-mail: yejian.lyu@sjtu.edu.cn).

Pekka Kyösti is with the Centre for Wireless Communications, University of Oulu, 90570 Oulu, Finland, and also with Keysight Technologies Finland Oy, 90590 Oulu, Finland (e-mail: pekka.kyosti@oulu.fi).

Digital Object Identifier 10.1109/TAP.2024.3489959

***Index Terms*— Angular dispersion, beamforming, radio channel characterization, sub-terahertz (sub-THz), time dispersion.**

I. Introduction

EXTENDING to the upper millimeter-wave (mmWave) or sub-terahertz (sub-THz) range (100–300 GHz), and in the future also to the THz range (>300 GHz) is expected to make extremely high data rate communication becoming reality in the 6G era [1]. Large-scale antenna arrays that offer high directive gain and beamforming capabilities are necessary to compensate for the severe signal attenuation at high frequency [2]. New radio interfaces must be designed and parameterized for future sub-THz communication systems.

Research work to address the challenges is ongoing, e.g., in the European Hexa-X and Hexa-X-II projects [3], [4]. For example, the waveform design is related to the delay spread (DS) and maximum excess delay (MED) of the *radio channel* observed by specific antenna beam patterns. In particular, the subcarrier spacing, cyclic prefix (CP) length in orthogonal frequency-division multiplexing (OFDM) system, and equalizer length in a single-carrier system, are typically determined based on the expected time dispersion parameters, i.e., root-mean-squared (RMS) DS and MED of that environment [5]. Also, the presence of channel angular spread may yield the degradation of beamforming performance due to a mismatch between the beam pattern and the angular spread around the main path direction. Consequently, with a limited number of radio frequency (RF) chains, the antenna array needs to be reconfigured to form the beam pattern matching with the angular spread of the radio channel [6]. In these respects, it is essential to analyze the angular and time dispersion of the radio channel in which the sub-THz system will operate, rather than those of the *propagation channel* where the impact of antenna beam pattern has been deembedded. Note that the radiation pattern of an antenna array strongly depends on the beamforming scheme, antenna elements, and array geometry. Thus, different beam patterns will formulate different radio channels when either the concentrated beams are steered to the desired directions or some more complex beamformers are used.

Previous measurement and simulation results show a significant reduction of beamforming gains owing to multipath

scattering, i.e., channel angular dispersion [7], [8]. In [6], an array geometry optimization scheme was proposed to match the beam pattern with the estimated angular spread for the system equipped with analog/hybrid beamforming and, in turn, increase the cell capacity. Besides, a high DS causes inter-symbol interference (ISI), which can be mitigated by inserting CP before data symbols. The robustness against ISI in high-frequency multicarrier systems is determined by the length of CP, where in general longer symbols are adopted in the environments with larger DS [9]. Similarly, in single-carrier systems with time-domain equalization, delay spread determines the required length of the equalizer. At the expense of lower spectral efficiency and longer transmission delay, optimizing waveform design strongly depends on the multipath DS of the radio channel [10].

From a radio channel characterization perspective, a *beam-weighted channel*, where measured multipath components (MPCs) of the corresponding propagation channel are weighted by a directive beam pattern steered to single and/or multiple directions, performs different angular and time dispersion characteristics in contrast to the omnidirectional or antenna-free propagation channel. As shown in Fig. 1, radio signal emanating from the transmitter (Tx) spreads out spatially and it travels along one line-of-sight (LOS) and two nonline-of-sight (NLOS) paths before being received by the receiver (Rx) antenna. Implementing high directive beamforming on the Rx side results in spatial filtering of the propagation channel, where the antenna radiation pattern is essentially the response of the spatial filter. For example, only two paths, i.e., paths #1 and #2, are visible for the main lobe of the beam pointing along the single dominant path #1, while only one path, i.e., path #3, is visible when steering the beam to the other direction. Then, path gains will be weighted with an array pattern at the corresponding directions, i.e., azimuth angle of arrival (AoA). Consequently, time dispersion parameters of beam-weighted channels potentially differ from those of isotropic channels. However, there is a lack of studies that focus on analyzing the beam pattern impact on multipath angular and time dispersion especially in measured sub-THz channels.

The narrower the beam the fewer significant MPCs can be observed, leading to the decrease of DS and MED. In [11], a comparison of the measured DS at 2.45 GHz in an indoor obstructed environment shows that using co-polarized directional antenna pairs provides smaller DS than using omnidirectional antenna pairs. In [12], the directional DS is calculated based on the power delay profile (PDP), which is synthesized from the power angular delay profile (PADP) within a certain angular range without weighting beam pattern. The corresponding range is determined by the half power beamwidth (HPBW) of the antenna and toward the direction providing the highest received power. In the multiple-input multiple-output (MIMO) case combined with beamforming technology, theoretical analysis indicates that there are several beamforming attributes, including antenna size, HPBW, sidelobe level, beam direction, and beam misalignment, that affect channel dispersion [10], [13]. There are two ways to include the beamforming impact when

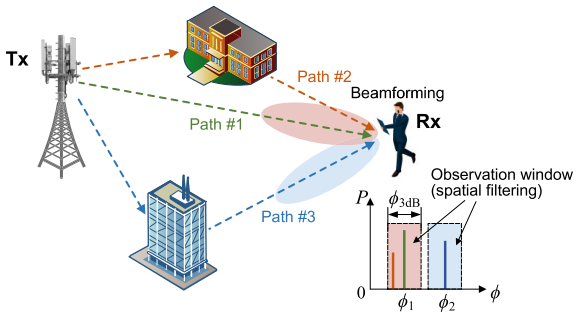

Fig. 1. Illustration of the radio channel observed via specific beam patterns and their impact on channel dispersion.

collecting MPCs of radio channels for the calculation of angular and time dispersion parameters: 1) if measurements are conducted using real or virtual antenna arrays, the impact of beamforming method is included inherently [14] or via postprocessing [15] during the estimation of beam-weighted MPCs. 2) The other way is to weight the propagation paths with desired beam patterns, which is applicable to any channel measurement data without prerequisites on the antenna configuration. The 5–60 GHz channel measurement results reported in [14] show that the reduction of DS as a function of HPBW becomes more obvious in outdoor environments with relatively larger DS values. Wyne et al. [15] analyzed the influence of different beamformers and array sizes on the DS and MED of measured 60-GHz channels using virtual antenna arrays. On the other hand, high-resolution directional channel measurement campaigns were conducted and the synthetic antenna patterns with variable beamwidths were applied in postprocessing at 60 GHz [16], [17]. The aforementioned empirical analyses, in general, were promoted to evaluate the beamforming impact on channel dispersion using beam patterns with different HPBWs.

In this article, we investigate the beamforming impact on angular and time dispersion based on extensive multiscenario sub-THz channel measurement data. Experimental and simulation results have revealed the spatial sparse nature of high-frequency channels, which benefits beam management in exploiting low-complexity methods [18]. Thus, beam patterns of direction-based beamformer are utilized to weight the propagation paths using the beam direction information estimated from measured sub-THz channels. In this context, the main contributions of this article can be summarized as follows.

1) A large amount of sub-THz propagation channel data have been collected across multiple scenarios. Estimated MPC parameters are utilized to analyze the impact of different beamformers on angular and time dispersion.
2) The postprocessing of the decoupled propagation channel data has been performed including three stages: 1) beam direction finding; 2) forming desired beam patterns; and 3) weighting propagation paths with steered beam patterns and calculating channel dispersion parameters.
3) Statistical analyses of the azimuth angle spread of arrival (ASA) of the beamformed channel and the time

dispersion parameters (i.e., DS and MED) of beam-weighted channels are performed to provide practical design insights on, e.g., novel waveforms and air interfaces.

In the remainder of this article, we first describe the details about the sub-THz propagation channel data collection across multiple environments in Section II. Section III details the data postprocessing methods for analyzing beamforming impact on the angular and time dispersion of directional channels. The statistical results of ASA, DS, and MED are presented in Section IV. Finally, Section V concludes this work with some remarks for system design.

II. Sub-THz Propagation Channel Data Collection

A. Measurement Setups

The 142-GHz propagation channel data used in this work were collected via single-directional channel measurements across several indoor and outdoor environments. The measurement campaigns were conducted at the center frequency of 142 GHz using vector network analyzer (VNA)-based channel sounder with the implementation of radio-over-fiber technology, as described in [19] and [20]. During the measurements, a 0-dBi omnidirectional bicone antenna with 45° elevation HPBW was fixed on the Tx side and a 19-dBi horn antenna with 10° azimuth HPBW and 40° elevation HPBW was used on the Rx side. The directional scanning sounding method was used with Rx horn antenna mounted on a rotator to capture directional channel information with the increment of 5°. Note that the Rx horn antenna was only rotated in the azimuth plane. More details about the measurement setups are described in the rest of this section and summarized in Table I.

B. Measurement Environments

Indoor 142-GHz propagation channel data were collected in the entrance hall [20]. A total of 28 LOS and 47 NLOS Tx–Rx links were measured with Tx and Rx antennas elevated up to 1.85 m above the floor. To reduce the measurement duration of each Tx–Rx link, Rx antenna was rotated within several specific angle ranges for different Rx locations as listed in Table I. The link distances are within 3–60 m.

Outdoor 140–144-GHz propagation channel data were collected in three environments, i.e., suburban area, residential area, and city center [21]. In the first two environments, Tx and Rx antennas were elevated to the same heights, i.e., 1.85 m, while in the third environment, they were at the height of 2 m. In total, 35, 23, and 12 LOS links were considered in the three environments, respectively, as well as 4, 38, and 23 NLOS links. The link distances range from 2 to 178 m. In terms of the antenna configuration, Rx horn antenna was rotated in 2π azimuth plane with 5° rotation step, while Tx omnidirectional was fixed on the top of the tripod. For each Tx–Rx link, a total of 72 single-directional channel frequency responses (CFRs) has been collected.

C. Data Preprocessing

According to the VNA-based channel sounding, angular-dependent channel impulse responses (CIRs) are derived by the inverse fast Fourier transform of directly measured CFRs with a rectangular window. For each Tx–Rx link, single-directional PDPs and PADP can be further derived based on angular-dependent CIRs. The MPCs can be detected as local peaks of the PADP in accordance with the following procedure: 1) detecting local maxima on the single-directional PDP; and then 2) looking for the greater maximum at the specified delay bins using the PADP. Here, a finer peak searching method is employed for the detection of local maxima. Such a method is performed via interpolation of the neighboring delay and angular bins using a peak-normalized gain pattern of the sinc function and the horn antenna, respectively. More details about MPCs estimation from measured CFRs can be found in [22].

Here, the antenna gain pattern is specified at every 1° so that the AoAs of MPCs can be estimated with 1° accuracy. Compared with raw data measured with the rotation step of 5°, the angular resolution of estimated MPCs has been improved. After deembedding the radiation patterns of the Rx horn antenna, we can extract MPC or path information of each Tx–Rx link, including the number of paths, path gain, propagation delay, and AoA. Furthermore, angular information from Tx side of each path can be obtained via the measurement-based ray-launcher (MBRL) based on the estimated single-directional path information on the Rx side. Using MBRL introduced in [20], [23], and [24], path information combined with the environment and location information is treated as the input to the MBRL and the output is the double-directional path angular information, e.g., azimuth angle of departure (AoD).

As the Rx was fixed at no more than three locations, we only moved Tx to several different locations during the measurements. Actually, the Rx and Tx defined in the 142-GHz measurements act as base station (BS) and user equipment (UE), respectively. Thus, the azimuth angular information obtained on the Tx side is treated as AoA. All outdoor propagation channel data is available in [21].

III. Data Postprocessing

Based on the sub-THz channel measurement and MPC estimation results, the PADP of each Tx–Rx link is written as

$$P(\tau, \phi) = \sum_{l=1}^{L} p_l \delta(\tau - \tau_l)\delta(\phi - \phi_l) \tag{1}$$

where L is the total number of MPCs and p_l, τ_l, and ϕ_l are the power, propagation delay, and AoA of the lth path, respectively, and $\delta(\cdot)$ is the Dirac delta function. Here, only single-directional channels with respect to the Rx side are considered. Note that the antenna gain has been deembedded when estimating the propagation path gain $\{p_l\}$ from propagation measurement data. Thus, the PADPs $P(\tau, \phi)$ jointly characterize the power distribution of propagation channels in both time and angular domains.

TABLE I
SUB-THz INDOOR AND OUTDOOR SINGLE-DIRECTIONAL CHANNEL MEASUREMENT SETUPS

Envi.	Indoor	Outdoor		
	Entrance hall	Suburban	Residential	City center
Freq. range [GHz]	140–144	140–144	140–144	140–144
Tx ant. height [m]	1.85	1.85	1.85	2.00
Rx ant. height [m]	1.85	1.85	1.85	2.00
Rx az. range [°]	Rx1: −90–180 Rx2: 40–250 Rx3: 110–290	0–355	Mostly 0–355	Mostly 0–355
Rx az. step [°]	5	5	5	5
Num. LOS links	28	35	23	12
Num. NLOS links	47	4	38	23
Link distance [m]	3–66	2–172	20–175	10–178

A. Beam Direction Finding

The wireless systems in practice operate in beamformed radio channels. The can be defined by taking the convolution of the propagation channel PADPs $P(\tau, \phi)$ and desired beam pattern $G(\phi)$ via

$$\begin{aligned}\hat{P}(\tau, \phi) &= \int P(\tau, \varphi)\, G(\phi - \varphi)\, \mathrm{d}\varphi \\ &= \sum_{l=1}^{L} p_l G(\phi - \phi_l)\delta(\tau - \tau_l).\end{aligned} \tag{2}$$

Compared with the $\phi \in \{\phi_l\}$ in the original measured PADPs $P(\tau, \phi)$, the $\phi \in [0°, 360°]$ in the beamformed PADP $\hat{P}(\tau, \phi)$ denotes the azimuth beam steering angle. In (2), we first steer the beam to each direction ϕ and calculate the sum gain of all weighted propagation path gains, where each MPC is weighted with the antenna gain at the corresponding direction. The sum of weighted MPCs is the beam power toward azimuth angle ϕ.

As shown in Fig. 2(a), the black circles denote the discrete propagation channel measurement data, i.e., MPCs. We first steer beams toward all azimuth angles in $[0°, 360°]$ with the increment of 1°. A simplified beam shape, i.e., 3GPP beam pattern defined in [25], can provide a finer HPBW granularity as

$$G(\phi)\ [\mathrm{dB}] = -\min\left\{12\left(\frac{\phi}{\phi_{3\mathrm{dB}}}\right)^2, 60\right\}, \quad \phi \in [-90°, 90°] \tag{3}$$

where $\phi_{3\mathrm{dB}}$ is the HPBW of the 3GPP beam pattern and the peak-to-minimum gain ratio is set as 60 dB. However, (3) represents an ideal beam pattern without sidelobes, which is often impractical. Instead, the beam response or beam pattern of a half-wavelength spaced ULA with N isotropic elements is considered with

$$G(\phi) = \mathbf{w}^{\mathrm{H}}\mathbf{a}(\phi), \quad \phi \in [-90°, 90°] \tag{4}$$

where $\mathbf{a}(\phi) = [1, \xi(\phi), \ldots, \xi^{N-1}(\phi)]^{\mathrm{T}}$ is the steering vector of N-element ULA corresponding to the angle ϕ with $\xi(\phi) = \exp(-j(2\pi d \sin\phi/\lambda))$, λ is the wavelength, and $d = \lambda/2$ is the element spacing. The superscripts $(\cdot)^{\mathrm{H}}$ and $(\cdot)^{\mathrm{T}}$ stand for the Hermitian transpose and transpose, respectively. The $\mathbf{w} = [w_1, w_2, \ldots, w_N]^{\mathrm{T}}$ is the weights vector with $w_n = 1$, $n \in [1, N]$. Here, the beam pattern $G(\phi)$ of a ULA with 16 elements is employed in Fig. 2(a). Note that the boresight of the ULA points along the direction of $\phi = 0°$ and the beam pattern is only defined for the boresight half-plane, i.e., $\phi \in [-90°, 90°]$, while the beam gain is set to a constant value of -60 dB for the back half-plane, i.e., $\phi \in [-180°, -90°] \cup [90°, 180°]$. The black line in Fig. 2(a) represents the beamformed power angular spectrum (PAS) $\hat{P}(\phi)$ with respect to the AoA calculated as $\hat{P}(\phi) = \sum_\tau \hat{P}(\tau, \phi)$.

Potential beam directions $\mathcal{A} = \{\phi_{\mathrm{b},m}\}$ with $\phi_{\mathrm{b},m} \in [0°, 360°)$ are estimated based on the local maxima of the beamformed PAS using peak detection algorithm. Here, only the beams whose power values are within a certain threshold $\Delta_{\mathrm{b,th}}$ below the global maximum power are taken into account. For example, the threshold of $\Delta_{\mathrm{b,th}} = 10$ dB is used for finding beam directions, as depicted in Fig. 2(a), where a total of two beam directions are detected, i.e., $M = \mathbf{card}(\mathcal{A}) = 2$. The operator $\mathbf{card}(\cdot)$ denotes the cardinality of a set. The maximum of these beam powers indicates the *max beam* direction

$$\phi_{\mathrm{b,max}} = \arg\max_{\phi_{\mathrm{b,m}}} \hat{P}(\phi_{\mathrm{b,m}}). \tag{5}$$

In Fig. 2(a), $\phi_{\mathrm{b,max}}$ is equal to $\phi_{\mathrm{b},1} = 156°$. Other prominent beams are included in *local maxima* (LM) *beams*, e.g., $\phi_{\mathrm{b},2} = 211°$ in Fig. 2(a).

B. Single-Direction Beamforming

Once beam direction set $\mathcal{A}$ is found, we will steer the same beam to different beam directions via $G(\phi - \phi_{\mathrm{b},m})$. The beam-weighted PADPs for the mth beam pointing angle is

$$\tilde{P}(\tau, \phi|\phi_{\mathrm{b},m}) = \sum_{l=1}^{L} p_l G(\phi_l - \phi_{\mathrm{b},m})\delta(\tau - \tau_l)\delta(\phi - \phi_l) \tag{6}$$

where $\tilde{p}_l = p_l G(\phi_l - \phi_{\mathrm{b},m})$ is the beam-weighted path gain along the direction of lth path. We can obtain the corresponding PAS via $\tilde{P}(\phi|\phi_{\mathrm{b},m}) = \sum_\tau \tilde{P}(\tau, \phi|\phi_{\mathrm{b},m})$. The black downward-pointing triangles in Fig. 2(b) represent the PAS $\tilde{P}(\phi|\phi_{\mathrm{b},1})$, which is weighted with the circular shift of $G(\phi)$ at the max beam direction of $\phi_{\mathrm{b},1}$, i.e., $G(\phi - \phi_{\mathrm{b},1})$ shown in Fig. 2(c) with the black solid line.

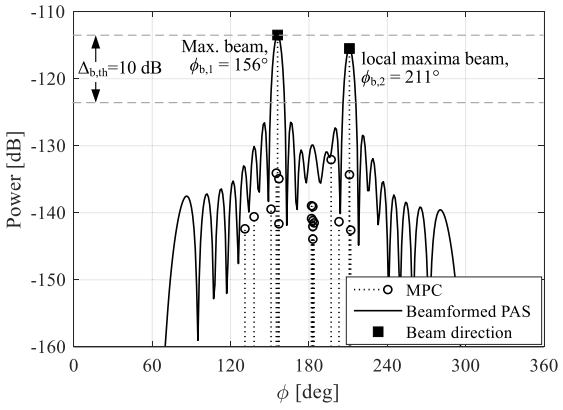

(a)

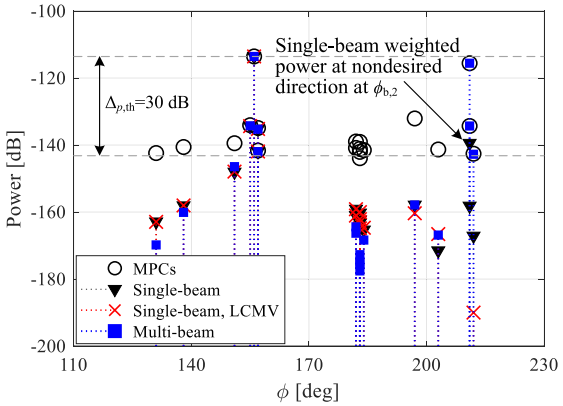

(b)

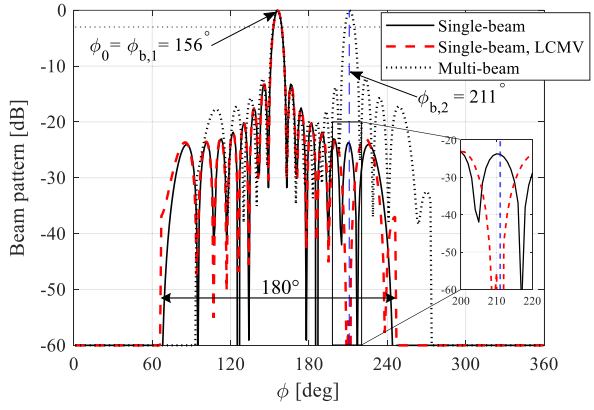

(c)

Fig. 2. Illustration of the data postprocessing procedures in an example link. Propagation paths, beam power, and selected beam directions in an example link. (a) Beamformed PAS and estimated beam directions. (b) Beam-weighted PAS at the desired beam pointing angle(s). (c) Single-beam and multibeam patterns of the uniform linear array (ULA) with $N = 16$ elements.

For single-direction beamforming case using the traditional beam pattern in (4), however, significant interference from the nondesired beam directions will potentially lead to an uncertain measure of ASA and DS, due to the contributions of antenna sidelobes. An instance of such case in Fig. 2(b) shows that the beam-weighted path gain at the nondesired beam direction $\phi_{b,2} = 211°$ is still within the power threshold $\Delta_{p,th}$ of 30 dB below the maximum path gain. Thus, the development of an optimal beamforming solution is needed to null out interferences from nondesired beam directions.

In the following, we will consider the optimal beamformer to form nulls in the direction of interferences. Denote $\phi_{b,i}$ for $m = i$ to be the desired single-beam direction, while $\{\phi_{b,m}\}$ for $m \neq i$ to be nulling directions. Here, a linear constraints minimum variance (LCMV) beamformer is adopted, where the objective is to minimize the total noise output while preserving the signal from $\phi_{b,i}$ and nulling out interferences from $\phi_{b,m}(m \neq i)$. The LCMV beamforming weight optimization problem is expressed as

$$\begin{aligned} &\min_{\mathbf{w}} \ \mathbf{w}^{\mathrm{H}}\mathbf{R}\mathbf{w} \\ &\text{s.t. } \mathbf{w}^{\mathrm{H}}\mathbf{a}(0) = 1 \\ &\quad \mathbf{w}^{\mathrm{H}}\mathbf{a}(\hat{\phi}_{b,m}) = 0 \end{aligned} \tag{7}$$

where $\mathbf{R} \in \mathbb{C}^{N\times N}$ is the spatial covariance matrix and $\hat{\phi}_{b,m} = \phi_{b,m} - \phi_{b,i}$ is defined as the nulling direction satisfying

$$|\hat{\phi}_{b,m}| = |\phi_{b,m} - \phi_{b,i}| < 90° \quad \forall m \in [1, M], \ m \neq i. \tag{8}$$

The first constraint represents that the response of the ULA is steered to the direction of 0° with unit gain; and the second constraint is applied to nullify the array response to signals from the directions in (8).

Assume that the total number of nulling directions is M_{null}, which satisfies $0 \leq M_{\text{null}} \leq M - 1$. The covariance matrix $\mathbf{R}$ can be written as [26]

$$\mathbf{R} = \sigma_w^2 \mathbf{I}_N \tag{9}$$

where σ_w^2 denotes the noise level and $\mathbf{I}_N$ is the $N \times N$ identity matrix. Here, the additive white Gaussian noise is considered. A closed-form solution of the optimal weight vector can be expressed as [26]

$$\mathbf{w}_o = \mathbf{C}\left(\mathbf{C}^{\mathrm{H}}\mathbf{C}\right)^{-1}\mathbf{g} \tag{10}$$

where the $N \times (M_{\text{null}} + 1)$ constraint matrix is $\mathbf{C} = [\mathbf{a}(0), \mathbf{a}(\hat{\phi}_{b,1}), \ldots, \mathbf{a}(\hat{\phi}_{b,M_{\text{null}}})]$ and the $(M_{\text{null}}+1)\times 1$ constraint vector is $\mathbf{g} = [1, 0, \ldots, 0]^{\mathrm{T}}$. Then, the beam pattern with the optimal weights $\mathbf{w}_o$ from the solution of (7) can be written as $G_o(\phi|\phi_{b,i}) = \mathbf{w}_o^{\mathrm{H}}\mathbf{a}(\phi)$ for $\phi \in [-90°, 90°]$, while for the back half-plane, i.e., $|\Delta\phi_{b,m}| \geq 90°$, the beam gain is set to a constant level of -60 dB. Instead of using the beam-weighted path gains in (6), when we alter the direction of the main lobe of the optimal array pattern to $\phi_{b,m}$, the l-th path gain is $\tilde{p}_l = p_l G_o(\phi_l - \phi_{b,m}|\phi_{b,i})$ with $m = i$. In theory, the classical LCMV beamformer can achieve perfect interference and noise cancellation when the precise channel state information is known, despite it poses challenges in a real-world implementation. Following the method proposed in this section, more practical beamforming schemes can be employed to analyze their impact on channel dispersion parameters for specific sub-THz systems.

As shown in Fig. 2(c), the red dashed line represents the circular shift of the optimal beam pattern $G_o(\phi_l - \phi_{b,1}|\phi_{b,1})$ toward the max beam direction $\phi_{b,1}$, while suppressing the interference from the direction of $\phi_{b,2}$. The corresponding path gains are also depicted in Fig. 2(b) with red crosses. Compared with the beam-weighted PAS without using the

optimal beamformer, the gains of the paths coming along the nulling direction, i.e., $\phi_{\mathrm{b},2} = 211°$, are significantly reduced considering LCMV beamformer. For example, the corresponding path gains are below the lower limit of the y-axis as used in Fig. 2(b).

C. Multidirection Beamforming

Multibeam MIMO operation is essential to increase the capacity of the system and effectively mitigate the impact of deep fading through spatial diversity. Multibeam antenna arrays with beamforming can focus the signal in multiple directions and simultaneously transmit multiple data streams over an MIMO channel. Here, the impact of the multibeam pattern is taken into consideration only when the desired beam directions satisfy

$$\mathcal{A}_{\mathrm{MB}} = \left\{\tilde{\phi}_{\mathrm{b},k} = \phi_{\mathrm{b},m} \middle| |\phi_{\mathrm{b},m} - \phi_{\mathrm{b,max}}| < 90° \right\}. \tag{11}$$

That is only the beam directions $\phi_{\mathrm{b},m}$ specified within the range from $\phi_{\mathrm{b,max}} - 90°$ to $\phi_{\mathrm{b,max}} + 90°$ are used for multidirection beamforming. Here, we refer $\tilde{\phi}_{\mathrm{b},k}$ as the beam directions satisfying the constraint in (11). The set $\mathcal{A}_{\mathrm{MB}}$ is the subset of $\mathcal{A}$ that includes all potential beam directions estimated based on beamfomred PASs, i.e., $\mathcal{A}_{\mathrm{MB}} \subseteq \mathcal{A}$. Thus, the cardinality of $\mathcal{A}_{\mathrm{MB}}$, i.e., $K = \mathbf{card}(\mathcal{A}_{\mathrm{MB}})$, is finite and less than or equal to M. Then the N-element ULA forms beams to K, $K \in [1, M]$ desired beam directions. The corresponding weight vector can be expressed as

$$\mathbf{w}_{\mathrm{MB}}^{\mathrm{T}} = \mathbf{g}\left(\mathbf{A}^{\mathrm{H}}\mathbf{A}\right)^{-1}\mathbf{A}^{\mathrm{H}} \tag{12}$$

where $\mathbf{g} = [g_1, g_2, \ldots, g_K]$, $g_k \in [0, 1]$ controls the power distribution among K beam directions and equal beam power allocation is used here, i.e., $g_k = (1/\sqrt{K})$. The matrix $\mathbf{A} \in \mathbb{C}^{N\times K}$ contains the steering vectors of the K beam directions

$$\mathbf{A} = \left[\mathbf{a}(\tilde{\phi}_{\mathrm{b},1}), \mathbf{a}(\tilde{\phi}_{\mathrm{b},2}), \ldots, \mathbf{a}(\tilde{\phi}_{\mathrm{b},K})\right]. \tag{13}$$

The multibeam pattern can, thus, be written as $G_{\mathrm{MB}}(\phi) = \mathbf{w}_{\mathrm{MB}}^{\mathrm{H}}\mathbf{a}(\phi)$. Similarly, the beam pattern for multidirection beamforming is only defined for the boresight half-plane, i.e., $\phi \in [\phi_{\mathrm{b,max}} - 90°, \phi_{\mathrm{b,max}} + 90°]$, and the constant beam gain of -60 dB is set for the back half-plane. If only one beam direction satisfies the constraint (11), single-direction beamforming is considered instead of multidirection beamforming.

The black dotted line in Fig. 2(c) represents the multibeam pattern focusing on two estimated beam directions $\phi_{\mathrm{b},1}$ and $\phi_{\mathrm{b},2}$. The corresponding beam-weighted PAS is depicted in Fig. 2(b) with blue squares.

D. Angular and Time Dispersion

The angular dispersion of beamformed channel is characterized by the RMS ASA based on beamformed PAS via [27]

$$\sigma_\phi = \sqrt{\frac{\sum_\phi \left|\exp(j\phi) - \mu_\phi\right|^2 \hat{P}(\phi)}{\sum_\phi \hat{P}(\phi)}} \tag{14}$$

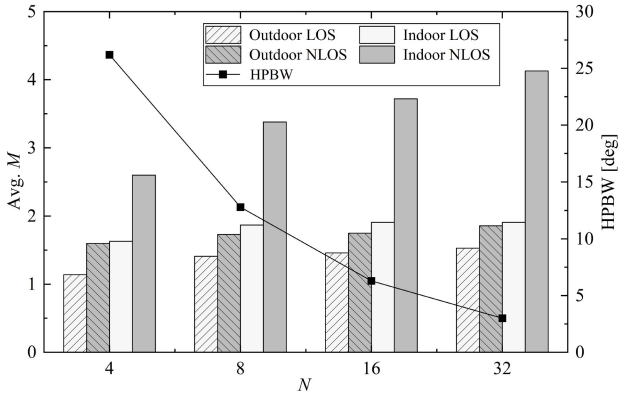

Fig. 3. Average numbers of beam directions finding by the ULAs with different number of elements. The black squares denote the HPBWs of ULAs with different numbers of elements.

and the mean angle is calculated as

$$\mu_\phi = \frac{\sum_\phi \exp(j\phi)\hat{P}(\phi)}{\sum_\phi \hat{P}(\phi)} \tag{15}$$

where the angles ϕ are in radians and beamformed PAS $\hat{P}(\phi)$ is obtained in Section III-A. Here, only $\hat{P}(\phi)$ falling within the 30-dB power threshold below the global maximum power of $\hat{P}(\phi)$ is used for calculating RMS ASA.

The time dispersion is characterized by the second central moment of the PDP, i.e., RMS DS, computed as

$$\sigma_\tau = \sqrt{\frac{\sum_l \tau_l^2 \tilde{p}_l}{\sum_l \tilde{p}_l} - \left(\frac{\sum_l \tau_l \tilde{p}_l}{\sum_l \tilde{p}_l}\right)^2} \tag{16}$$

where the PDP is obtained via $\tilde{P}(\tau|\phi_{\mathrm{b},m}) = \sum_\phi \tilde{P}(\tau, \phi|\phi_{\mathrm{b},m})$. In addition, the MED can be calculated as

$$\tau_{\mathrm{MED}} = \max_{i,j\in[1,L]} |\tau_i - \tau_j|. \tag{17}$$

As mentioned earlier, only the paths whose beam-weighted path gains are within the $\Delta_{p,\mathrm{th}} = 30$-dB power threshold below the global maximum path gain $\max_l \tilde{p}_l$ are used in (16) and (17). Moreover, when we calculate the RMS ASA and DS of omnidirectional propagation channels, $\hat{P}(\phi)$ and $\tilde{p}_l$ in (14)–(16) are replaced with $P(\phi) = \sum_\tau P(\tau, \phi)$ and p_l, respectively.

IV. Results and Discussion

In this section, statistical analyses of the angular and time dispersion characteristics are presented using the beam patterns generated by ULAs with different numbers of elements, e.g., $N = 4$, 8, 16, and 32. In addition, we also adopt the 3GPP beam pattern proposed in [25] to mitigate the impact of sidelobe on channel dispersion.

A. Number of Beam Directions

Fig. 3 depicts the number of beam directions M estimated based on the beamformed PADPs $\hat{P}(\tau, \phi)$ using the method described in Section III-A. In general, more beams can be extracted from NLOS channel data compared with the LOS

results in both indoor and outdoor environments. Increasing the number of elements N decreases the HPBW of the corresponding half-wavelength spaced ULA, which results in more detectable beam directions, as shown in Fig. 3. This phenomenon gives rise to the fact that a narrower beam with smaller HPBW, i.e., higher spatial resolution, is able to discern between two beam directions in close proximity. In the presence of a well-separated multipath, however, the averaged numbers of estimated beam directions over all links in specific scenarios do not increase significantly with decreasing HPBW. Thus, as the HPBW of ULA decreased from 26.2° to 3°, only the beam directions in indoor NLOS scenario that exist more MPCs increase noticeably.

Moreover, except for the indoor NLOS case, the mean values of M are smaller than 2 indicating that sub-THz radio channels observed by specific beam patterns are sparse. Also, the same results can be found in [28], where the numbers of potential beam directions for most indoor 142-GHz links are smaller than 3 using the same $\Delta_{\text{b,th}} = 10$ threshold. Note that the number of beam directions to be nulled out (i.e., for optimal single-beam case) or simultaneously focused (i.e., for multibeam case) is smaller than the number of elements.

B. Angular Spread of Beamformed Channel

Owing to scattering in the environment, the radio channel observed by practical beam pattern, i.e., beamformed radio channel, will be *widened*, resulting in the reduction of effective antenna/beamforming gain. Such effect has been observed based on field measurement at 2.9 GHz [7] and 28 GHz [6]. Therefore, in this section, we would like to evaluate how severely the beam patterns of ULAs with different numbers of elements will affect the angular spread of the beamformed radio channel at sub-THz frequencies, compared with the angular spread of propagation channel. If the difference of angular spread between the beamformed channel and propagation channel becomes significant, dynamic directional beam configuration developed in [6] is necessary to match the antenna beam pattern with the channel, and further improve the link budget.

We first compare the empirical cumulative distribution functions (CDFs) of the RMS ASAs calculated based on measured PASs of propagation channels $P(\phi)$ and beamformed PASs of radio channels $\hat{P}(\phi)$, respectively. Since the propagation channel does not account for the impact of antennas or beams, we can assume that it is directly observed by omnidirectional antennas at both ends of the link, without any continuous beam steering as has been done when forming the beamformed channel. In this context, we use *omni* to refer to the results derived from the propagation channel. As shown in Fig. 4, the ASAs for NLOS links are larger than these for LOS links in both indoor and outdoor environments. Compared with the ASAs of the propagation channels, the ASAs of the beamformed channels observed by different ULAs will be widened by the beam patterns. Meanwhile, the beamformed ASAs generally decreases with increasing HPBWs of the ULAs by changing the number of elements (e.g., $N = 4$, 8, 16, and 32), especially for the

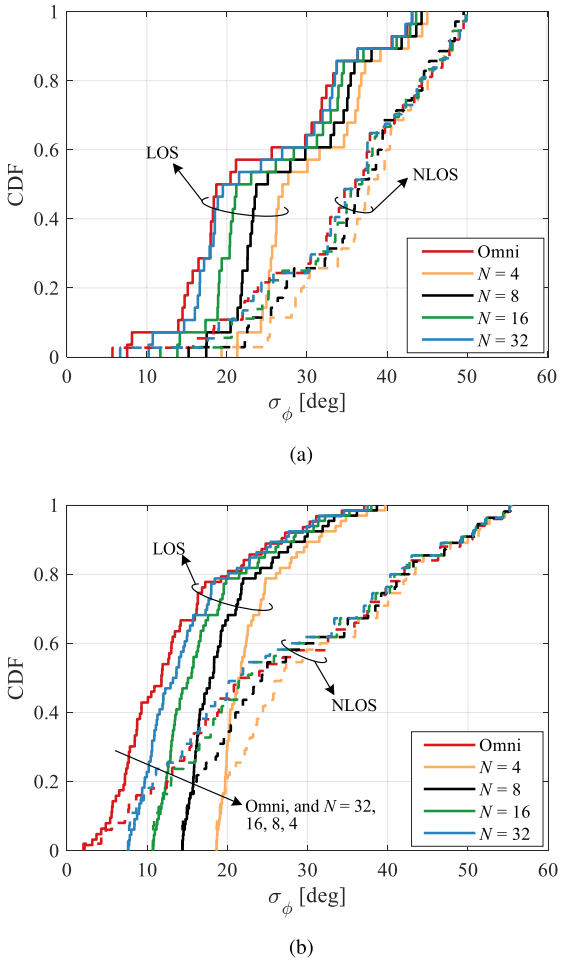

Fig. 4. Empirical CDFs of the RMS ASAs for propagation channels and beamformed channels calculated based on $P(\tau)$ and $\hat{P}(\tau)$, respectively. (a) Indoor. (b) Outdoor. The solid and dashed lines represent the results in LOS and NLOS scenarios, respectively.

links with small ASA values. It is also important to notice that NLOS links have much larger ASA than LOS in terms of propagation channel; however, the beamforming impact on ASA becomes less sensitive to the HPBWs of ULAs for these links having larger ASA. In other words, for the sub-THz link with small ASA, the ASA of the beamformed channel observed by practical beam pattern becomes larger than that of the propagation channel, especially when using the beam pattern with larger HPBW.

C. Comparison of Time Dispersion Parameters

The RMS DSs σ_τ and MEDs τ_{MED} of all indoor and outdoor omnidirectional propagation channels over Tx–Rx separation distances are illustrated in Fig. 5. Note that a 30-dB power threshold below the global maximum path gain is used to include only effective paths in the calculation of delay parameters. For each scenario, both delay parameters generally reduce as Rx moving far away from Tx. The σ_τ values for outdoor environment are slightly larger than those for indoor environment. With regard to τ_{MED}, however, we can notice pronounced differences between indoor and outdoor environments. The highest MEDs are among outdoor links,

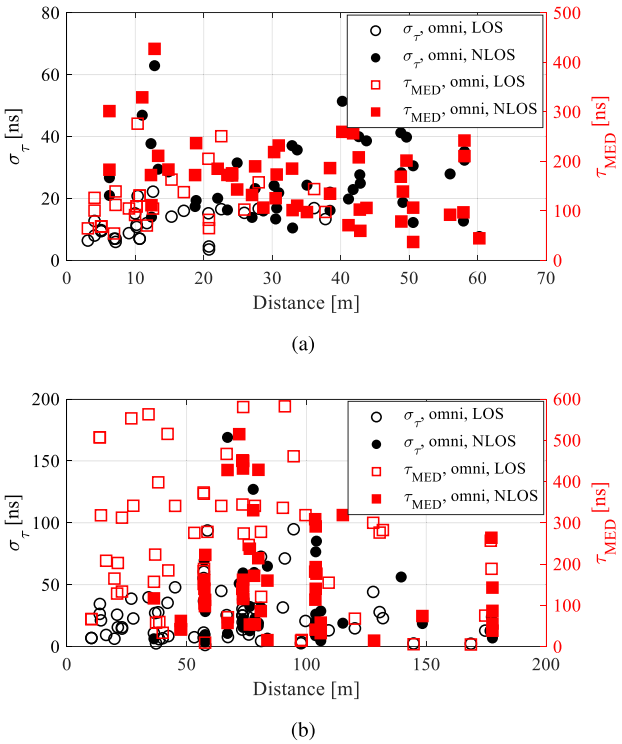

Fig. 5. Comparison of omni DSs (left axis) and MEDs (right axis) over link distances in (a) indoor and (b) outdoor environments, respectively.

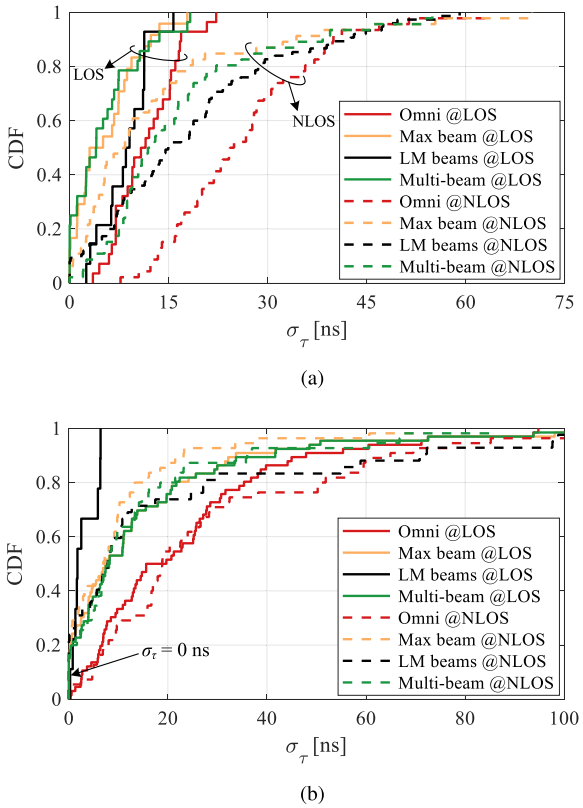

Fig. 6. Empirical CDFs of RMS DSs for the channels weighted by four-element ULA pattern in (a) indoor and (b) outdoor environments.

approaching close to 600 ns, while for indoor links, the MEDs values are always below 450 ns. Overall, without beam pattern weighting, large MEDs of omnidirectional propagation channels will cause a high level of ISI and in turn reduce spectral efficiency if longer CP is used in OFDM systems.

In Fig. 6, we compare the time dispersion parameters of the beam-weighted channels calculated based on beam-weighted PDP $\tilde{P}(\tau)$ for the max beam, LM beams, and multibeam cases. Here, the optimal single-beam patterns derived from the LCMV beamformer are utilized if the desired single-beam direction and the interfering beam directions satisfy the constraints in (7). The *max beam* denotes the case when propagation paths are weighted with the beam pattern pointing toward the max beam direction $\phi_{\text{b,max}}$, i.e., the direction providing the highest channel gain. The *LM beam* denotes the case when propagation paths are weighted with the single-beam pattern pointing toward other $M-1$ estimated beam directions within $\mathcal{A}$. The *multibeam* denotes the case when propagation paths are weighted with the multidirection beam pattern generated from Section III-C. Also, the *omni* refers to the case that no beam is formed, and hence, propagation paths are considered without any weighting by antenna beam patterns. To clearly show the differences in time dispersion parameters over four cases, identical beam patterns generated by four-element ULA are taken into account, rather than using narrower beams generated by larger ULAs.

The CDFs of RMS DSs σ_τ for indoor and outdoor environments are depicted in Fig. 6(a) and (b), respectively, where outdoor omni DSs are distributed in a larger interval. Compared with the results between LOS and NLOS scenarios, omni DSs for NLOS links are much larger than those for LOS links. As expected, the beam-weighted DSs are almost always smaller than those of the omni case. Meanwhile, the LM beams may provide even higher DSs in some occasions where the actual LOS path is not necessarily illuminated by the beam. Considering only the beam directions satisfying the constraint in (11) are illuminated, multibeam DSs are always larger than max beam DSs, whereas there is insufficient evidence to conclude the relationship between the DSs for multidirection and LM beam-weighted channels. From Fig. 6 we can also observe that beam steered DS for many links equals zero, e.g., for outdoor environment close to 20%. This is due to the fact that the corresponding links contain only a single path whose beam-weighted path gain is within the 30-dB power threshold and, in turn, the beam steered DS equals zero.

The statistics of MEDs τ_{MED}, including mean, median, and 90th-percentile values, are summarized in Table II which are differentiated by the environment, scenario, and beam-weighted case. Regarding the same scenario, outdoor propagation channels without weighing beam patterns exist higher MEDs. After weighing the propagation paths with desired beam patterns, the MED values are significantly reduced, leading to further improvement of OFDM transmission efficiency by using shortened CP. Different from DSs across three beam-weighted cases, no clear trend can be observed in terms of MEDs, indicating they strongly depend on the environment and scenario.

TABLE II
STATISTICS OF THE MED FOR DIFFERENT CASES USING THE BEAM PATTERN OF FOUR-ELEMENT ULA

Envi.	Scen.	Case	Descriptive statistics [ns]		
			Mean	Median	90-percentile
Indoor	LOS 142 GHz	Omni	119.10	106.91	192.53
		Max beam	66.41	45.46	156.94
		LM beams	98.44	100.34	157.76
		Multi-beam	62.92	45.87	150.26
	NLOS 142 GHz	Omni	166.28	172.23	255.12
		Max beam	107.38	96.80	210.00
		LM beams	112.70	96.68	218.63
		Multi-beam	112.47	102.32	204.55
Outdoor	LOS 142 GHz	Omni	246.04	240.46	503.14
		Max beam	149.61	70.36	341.72
		LM beams	88.58	43.29	279.11
		Multi-beam	151.03	70.36	341.72
	NLOS 142 GHz	Omni	159.13	116.83	427.96
		Max beam	64.19	41.04	145.74
		LM beams	80.78	40.91	202.91
		Multi-beam	71.12	42.49	168.73

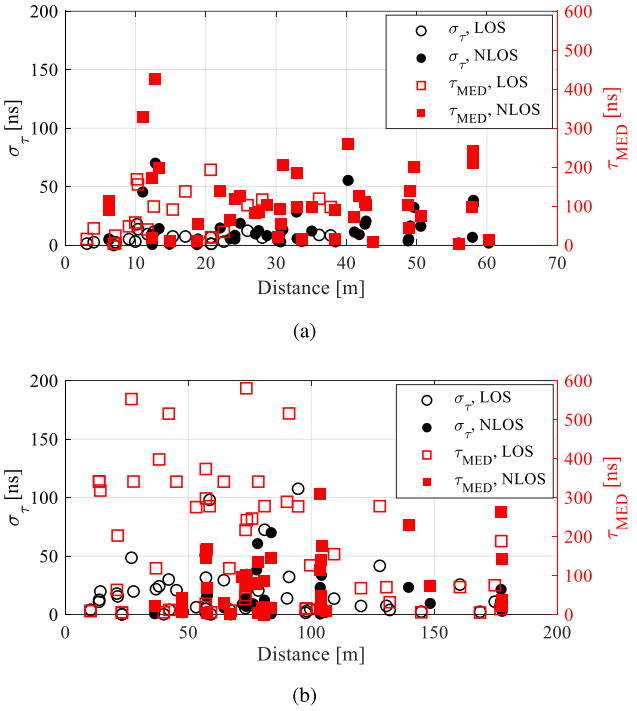

Fig. 7. Comparison of max beam DSs (left axis) and MEDs (right axis) over link distances in (a) indoor and (b) outdoor environments, respectively.

D. Impact of Max Single-Direction Beamforming

In Section IV-C, we compare the time dispersion parameters for omni, max beam, LM beams, and multibeam cases using identical beam patterns. However, owing to the severe propagation loss, sub-THz communications will probably only direct the signals toward a specific direction with the highest path gain. Consequently, in this section, we focus on investigating the impact of max single-direction beamforming on time dispersion parameters and how these parameters vary with the HPBW of different beam patterns.

The distance dependence of the max beam DSs and MEDs are shown in Fig. 7. Evidently, outdoor links are longer and the higher DS values can be found among them. However, any clear tendency of the max beam-weighted DS over link distance cannot be observed. Surprisingly, the NLOS DSs are not clearly higher than those of LOS links after weighting the propagation paths with steered max beam pattern. The largest MEDs are among outdoor links, but not in the links with the longest Tx–Rx distance. By visual inspection, the max beam-weighted MEDs for outdoor LOS links generally reduces with increasing link distances, while for other links no strong correlation between MED and link distance can be observed. Comparison between the results from LOS and NLOS scenarios indicates that LOS max beam MEDs for outdoor short-distance ($<$ 100 m) links are higher than those of NLOS links, however, opposite trend can be seen in Fig. 7(a) due to existing more detectable paths in NLOS scenarios.

Table III summarizes the mean, median, and 90th percentile DS and MED statistics calculated based on single-beam-weighted path gains $\tilde{p}_l$ with the four-element ULA beam pattern, which is steered to the max beam direction $\phi_{\text{b,max}}$. Notice that there were neither indoor links with Tx–Rx spacing above 100 m nor outdoor NLOS links with below 20-m spacing. Moreover, considering the number of measured links per environment, scenario, and distance category is small in some cases, the confidence of categorized statistics is, thus, not in all cases high. For indoor environments, no significant distance-dependency of DS can be observed when focusing single-beam along the max beam direction. However, for outdoor environment, the statistics of DS for links within $[20, 100]$ m are larger than those of short-distance ($<$ 20 m) links, while if Rx moving far from the Tx, max beam DS reduces with increasing link distance.

Here, we investigate the impact of HPBW on max beam DS and MED. The CDFs of RMS DSs and MEDs of the maximum beam weighted channels are illustrated in Fig. 8, where solid and dashed lines represent DS and MED, respectively. All analyzed 142-GHz links are treated without differentiating the environment and scenario. As the number of elements N in the ULA increases from 4 to 8, 16, and 32, the corresponding HPBW decreases from 26.2° to 12.8°, 6.3°, and 3°. As we expected, the CDF curve becomes shifted toward smaller DS and MED values. Normally, the narrower the beam, the fewer interacting objects can be illuminated by the beam, and the smaller DS and MED can be observed from a beam-weighted channel. The analysis indicated a clear inverse proportionality between HPBW and time dispersion parameters, i.e., DS σ_τ and MED τ_{MED}. In addition, there is a significant difference by comparing the probabilities that DS and MED values equal zero. From Fig. 8, more and more Tx–Rx links only exist one path with sufficient beam-weighted path gain as the increase of antenna size.

To evaluate the impact of HPBW on the time dispersion of measured sub-THz channels, we employ the 3GPP beam pattern defined in (3), which can provide a finer HPBW

TABLE III
STATISTICS OF THE MAX BEAM DS AND MED FOR DIFFERENT CASES USING THE BEAM PATTERN OF FOUR-ELEMENT ULA

Envi.	Scen.	Para.	Link dist $\leq$ 20 m			20 m $<$ Link dist $\leq$ 100 m			Link dist $>$ 100 m		
			Mean	Median	90-percentile	Mean	Median	90-percentile	Mean	Median	90-percentile
Indoor	LOS 142 GHz	σ_τ	5.22	2.75	13.37	5.96	6.58	11.21	-	-	-
		τ_{MED}	55.63	41.49	153.83	87.98	100.14	171.02	-	-	-
	NLOS 142 GHz	σ_τ	15.55	5.32	57.74	12.21	8.65	31.87	-	-	-
		τ_{MED}	142.14	102.32	378.15	97.73	96.80	204.95	-	-	-
Outdoor	LOS 142 GHz	σ_τ	5.69	3.95	16.89	17.37	9.45	47.10	12.14	7.41	32.06
		τ_{MED}	113.34	9.21	341.69	171.57	118.72	395.59	87.43	70.25	224.33
	NLOS 142 GHz	σ_τ	-	-	-	10.83	8.02	21.55	8.78	6.81	23.21
		τ_{MED}	-	-	-	54.92	42.16	134.80	79.19	39.87	242.89

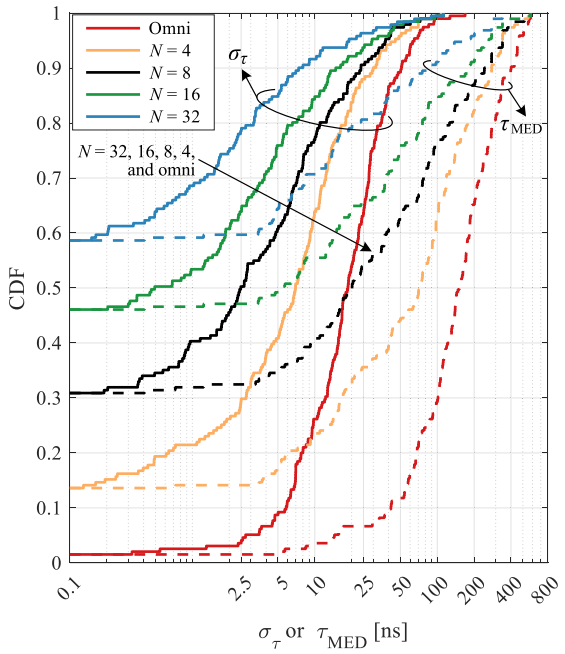

Fig. 8. Empirical CDFs of max beam DSs and MEDs for 142-GHz radio channels weighted by beam patterns of N-element ULAs. The solid and dashed lines represent the DS and MED results, respectively.

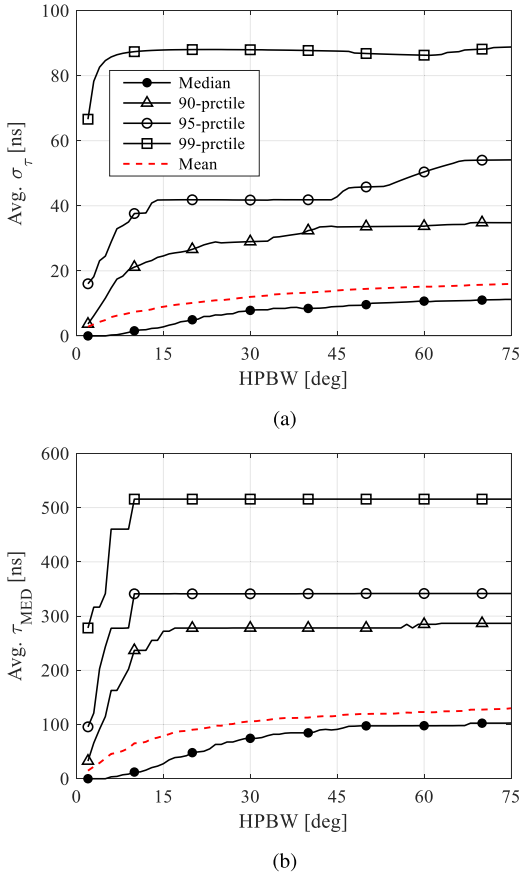

Fig. 9. Average (a) RMS DSs and (b) MEDs of all 142-GHz indoor and outdoor links versus HPBWs of the 3GPP beam patterns.

granularity. The statistics of RMS DSs and MEDs over all 142-GHz indoor and outdoor links are depicted in Fig. 9 as the function of HPBW. We can observe almost monotonically increasing mean values of DSs and MEDs with HPBW increasing from 2° to 75°. Moreover, compared with the 90th, 95th, and 99th percentiles of DSs and MEDs on average, they dramatically increase within the HPBW range of $[2°, 15°]$ and remain stable when the beam becomes much wider. Thus, if much wider beams are employed for sub-THz communications, it is possible to infer the time dispersion parameters of beam-weighted channels based on the previous analyses of four-element ULA pattern-weighted radio channels, considering the corresponding HPBW, i.e., 26.2°, is already within the stable region. As a curiosity, we can also observe that the mean and median curves of DSs and MEDs start converging with increasing HPBW, i.e., their corresponding probability distribution functions become symmetric with wider beams.

E. Impact of Sidelobes

To investigate the impact of sidelobes of the beam on time dispersion parameters, we compare the time dispersion statistics over max and LM beams weighted by the 3GPP beam pattern in (3) and the beam pattern of N-element ULA with half-wavelength spacing in (4), respectively. Despite advanced beamformers with amplitude tapering being more practical and useful, the 3GPP beam pattern can be regarded as an ideal case without sidelobes. Moreover, it facilitates fair comparison of sidelobe impact while maintaining the same HPBW. For example, as depicted in Fig. 10(a), the same HPBW, i.e., $\phi_{3\,\text{dB}} = 26.2°$, is selected for 3GPP beam pattern as that of the four-element ULA pattern. The 3GPP beam pattern having the

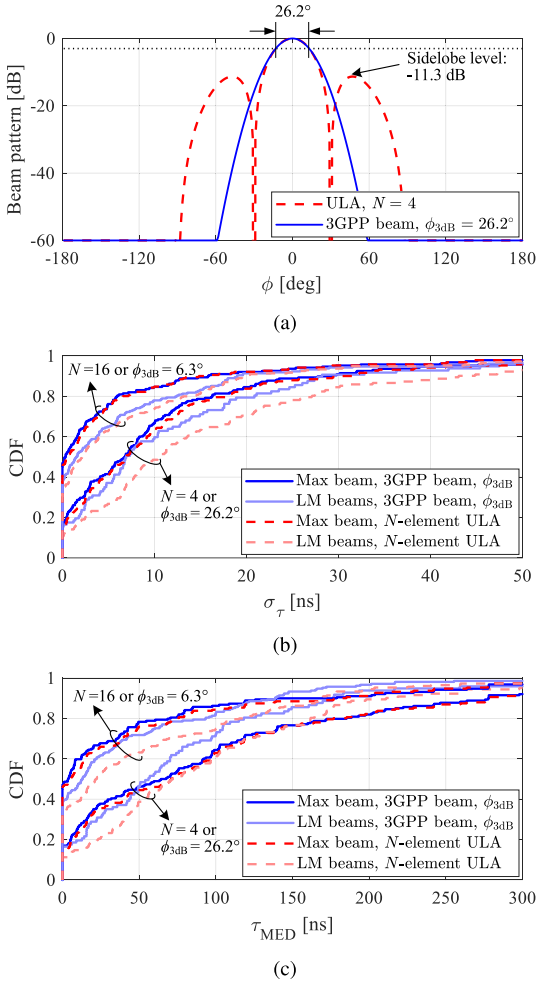

Fig. 10. (a) Comparison of the 3GPP beam pattern and four-element ULAs pattern with the same HPBW. Empirical CDFs of (b) RMS DSs and (c) MEDs over all 142-GHz indoor and outdoor links considering the impact of sidelobes.

same HPBW with 16-element ULA pattern, i.e., $\phi_{3\,\mathrm{dB}} = 6.3°$, is considered as well. The sidelobe level of four-element ULA pattern is about -11.3 dB below the maximum radiation of the main lobe [see Fig. 2(c)], and -13.2 dB for 16-element ULA pattern, which are both within the 30-dB threshold for delay parameter calculation.

Fig. 10(b) and (c) compares the empirical CDFs of RMS DSs and MEDs for both max beam and LM beams cases, respectively. In general, both DS and MED values increase when including sidelobes for beam weighting, whereas the extent of this increase is not pronounced. Since only the beam directions whose received powers are above a 10-dB threshold below the global maximum of beamformed PAS are taken into consideration, we already avoid the impact of antenna sidelobes in the process of beam direction estimation. Consequently, the difference between the resulting beam-weighted time dispersion parameters using two beam patterns is not significant, as depicted in Fig. 10. Besides, similar trends can be observed for the case using narrower beams, e.g., with the HPBW of 6.3°. As the 3GPP beam pattern represents an extreme case without sidelobes, the differences in time dispersion parameters of beam-weighted channels are expected to be less stark when using the beamformers with amplitude tapering.

V. Conclusion

In this article, we investigate how angular and time dispersion of measured sub-THz channels is affected by direction-based beamforming schemes along with varying beam patterns. Postprocessing of measured data has been performed for analysis of beamforming impact on channel dispersion characteristics. We first embed the beam patterns formed by the ULAs composed of different numbers of elements or simple 3GPP beam patterns on propagation paths. These paths are extracted from extensive sub-THz channel measurement data across multiple scenarios. We further analyze the resulting channel dispersion parameters statistics for the radio interface design.

Regarding the beamformed channel induced by spatial scanning, the resulting RMS ASAs are widened in contrast to the ASAs of the propagation channel. Such impact becomes more evident for LOS links having smaller ASA, especially when comparing the low percentiles of ASA values. A significant difference between the ASA of the beamformed channel and propagation channel indicates that dynamic directional beam configuration becomes necessary to improve sub-THz link budget.

Design aspects, such as equalizer length, subcarrier spacing, and CP length, are determined by the expected time dispersion parameters of the radio channel. After the inclusion of beam weights, RMS DS and MED statistics are presented in various categories combining indoor/outdoor, LOS/NLOS, and three-link distance classes. For example, the median DS and MED of the max beam over all measured links with 26.2° HPBW are 7.23 ns and 71.03 ns, respectively. The corresponding median values without beam impact, i.e., with an omnidirectional antenna, are 18.62 and 154.89 ns, respectively. Evidently, such a narrow beam pattern has a substantial impact on practical time dispersion characteristics. We also show the HPBW versus DS and MED trend of how the narrowing beamwidth yields shorter time dispersion, especially within the HPBW range of [2°, 15°]. Finally, a comparison between the results using 3GPP and ULA beam patterns with the same HPBW reveals that the sidelobe level has not resulted in a remarkable increase of DS and MED statistics.

References

[1] A. Pärssinen et al., "White paper on RF enabling 6G—Opportunities and challenges from technology to spectrum," 6G Flagship, Univ. Oulu, Oulu, Finland, White paper 13, Apr. 2021. [Online]. Available: http://urn.fi/urn: isbn:9789526228419

[2] A. L. Swindlehurst, E. Ayanoglu, P. Heydari, and F. Capolino, "Millimeter-wave massive MIMO: The next wireless revolution?" *IEEE Commun. Mag.*, vol. 52, no. 9, pp. 56–62, Sep. 2014.

[3] A. Nimr. (Mar. 2023). *D2.3 Radio Models and Enabling Techniques Towards Ultra-High Data Rate Links and Capacity in 6G*. [Online]. Available: https://hexa-x.eu/deliverables/

[4] P. Porambage and S. Kerboeuf. (Jun. 2023). *D2.1 Draft Foundation for 6G System Design*. Hexa-X-II Deliverable. [Online]. Available: https://hexa-x-ii.eu/deliverables/

[5] A. F. Molisch, *Wireless Communications*, 2nd ed., New York, NY, USA: Wiley, 2011.

[6] J. Du, M. Rybakowski, K. Bechta, and R. A. Valenzuela, "Matching in the air: Optimal analog beamforming under angular spread," 2019, *arXiv:1910.11054*.

[7] L. J. Greenstein and V. Erceg, "Gain reductions due to scatter on wireless paths with directional antennas," *IEEE Commun. Lett.*, vol. 3, no. 6, pp. 169–171, Jun. 1999.

[8] L. Ping'an and H. Yi, "Effects of angle spread on beamforming in wireless communications," in *Proc. Int. Conf. Wireless Commun., Netw. Mobile Comput.*, vol. 1, Wuhan, China, Sep. 2005, pp. 615–618.

[9] A. A. Al-jzari, I. Kostanic, and K. H. M. Mabrok, "Effect of variable cyclic prefix length on OFDM system performance over different wireless channel models," *Universal J. Commun. Netw.*, vol. 3, no. 1, pp. 7–14, Feb. 2015.

[10] B. Akgun, M. Krunz, and D. Manzi, "Impact of beamforming on delay spread in wideband millimeter-wave systems," in *Proc. Int. Conf. Comput., Netw. Commun. (ICNC)*, Big Island, HI, USA, Feb. 2020, pp. 890–896.

[11] C. Ho and T. Rappaport, "Effects of antenna polarization and beam pattern on multipath delay spread and path loss in indoor obstructed wireless channels," in *Proc. Int. Conf. Universal Pers. Commun. (ICUPC)*, Dallas, TX, USA, Sep. 1992, pp. 92–95.

[12] M.-D. Kim, J. Liang, H.-K. Kwon, and J. Lee, "Directional delay spread characteristics based on indoor channel measurements at 28GHz," in *Proc. IEEE 26th Annu. Int. Symp. Pers., Indoor, Mobile Radio Commun. (PIMRC)*, Hong Kong, Aug. 2015, pp. 403–407.

[13] H. Yang, M. H. A. J. Herben, I. J. A. G. Akkermans, and P. F. M. Smulders, "Impact analysis of directional antennas and multiantenna beamformers on radio transmission," *IEEE Trans. Veh. Technol.*, vol. 57, no. 3, pp. 1695–1707, May 2008.

[14] A. Simonsson, H. Asplund, J. Medbo, and K. Werner, "Beamforming impact on time dispersion assessed on measured channels," in *Proc. IEEE 87th Veh. Technol. Conf. (VTC Spring)*, Porto, Portugal, Jun. 2018, pp. 1–6.

[15] S. Wyne, K. Haneda, S. Ranvier, F. Tufvesson, and A. F. Molisch, "Beamforming effects on measured mm-wave channel characteristics," *IEEE Trans. Wireless Commun.*, vol. 10, no. 11, pp. 3553–3559, Nov. 2011.

[16] R. Sun, P. B. Papazian, J. Senic, C. Gentile, and K. A. Remley, "Angle- and delay-dispersion characteristics in a hallway and lobby at 60 GHz," in *Proc. 12th Eur. Conf. Antennas Propag. (EuCAP)*, Apr. 2018, pp. 1–5.

[17] R. Sun et al., "Millimeter-wave radio channels vs. synthetic beamwidth," *IEEE Commun. Mag.*, vol. 56, no. 12, pp. 53–59, Dec. 2018.

[18] H. Yan, V. Boljanovic, and D. Cabric, "Tracking sparse mmWave channel: Performance analysis under intra-cluster angular spread," in *Proc. IEEE 19th Int. Workshop Signal Process. Adv. Wireless Commun. (SPAWC)*, Kalamata, Greece, Jun. 2018, pp. 1–5.

[19] S. L. H. Nguyen, J. Järveläinen, A. Karttunen, K. Haneda, and J. Putkonen, "Comparing radio propagation channels between 28 and 140 GHz bands in a shopping mall," in *Proc. 12th Eur. Conf. Antennas Propag. (EuCAP)*, London, U.K., Apr. 2018, pp. 1–5.

[20] M. F. De Guzman, P. Koivumäki, and K. Haneda, "Double-directional multipath data at 140 GHz derived from measurement-based ray-launcher," in *Proc. IEEE 95th Veh. Technol. Conf. (VTC-Spring)*, Helsinki, Finland, Jun. 2022, pp. 1–6.

[21] M. F. De Guzman, K. Haneda, and P. Kyösti, Feb. 2023, "Measurement-based MIMO channel model at 140 GHz (V1)," Zenodo, doi: 10.5281/ZENODO.7640353.

[22] K. Haneda, S. L. H. Nguyen, J. Järveläinen, and J. Putkonen, "Estimating the omni-directional pathloss from directional channel sounding," in *Proc. 10th Eur. Conf. Antennas Propag. (EuCAP)*, Davos, Switzerland, Apr. 2016, pp. 1–5.

[23] M. Zhu, A. Singh, and F. Tufvesson, "Measurement based ray launching for analysis of outdoor propagation," in *Proc. 6th Eur. Conf. Antennas Propag. (EUCAP)*, Prague, Czech Republic, Mar. 2012, pp. 3332–3336.

[24] M. Francis De Guzman and K. Haneda, "Analysis of wave-interacting objects in indoor and outdoor environments at 142 GHz," *IEEE Trans. Antennas Propag.*, vol. 71, no. 12, pp. 9838–9848, Dec. 2023.

[25] *Study on Channel Model for Frequencies From 0.5 to 100 GHz*, document 38.901 (V17.0.0), 3GPP, Mar. 2022.

[26] H. L. V. Trees, *Optimum Waveform Estimation*. New York, NY, USA: Wiley, 2002, ch. 6, pp. 428–709.

[27] B. H. Fleury, "First- and second-order characterization of direction dispersion and space selectivity in the radio channel," *IEEE Trans. Inf. Theory*, vol. 46, no. 6, pp. 2027–2044, Sep. 2000.

[28] P. Kyösti, M. F. De Guzman, K. Haneda, N. Tervo, and A. Pärssinen, "How many beams does sub-THz channel support?" *IEEE Antennas Wireless Propag. Lett.*, vol. 21, pp. 74–78, 2022.

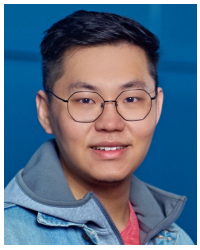

Peize Zhang (Member, IEEE) received the B.S. degree from the Beijing University of Posts and Telecommunications, Beijing, China, in 2015, the M.S. degree from the China Academy of Telecommunications Technology, Beijing, in 2018, and the Ph.D. degree (Hons.) from Southeast University, Nanjing, China, in 2022, all in electrical engineering.

From 2016 to 2018, he was a Research Assistant with the China Academy of Information and Communications Technology, Beijing, China. In 2021, he was a Visiting Ph.D. Student with the Université Catholique de Louvain, Louvain-la-Neuve, Belgium. Since 2022, he has been a Post-Doctoral Researcher in the 6G Flagship Programme with the Centre for Wireless Communications, University of Oulu, Oulu, Finland. From May to October 2024, he was a Visiting Research Fellow with Lund University, Lund, Sweden. His current research interests include propagation, deployment, and performance issues of millimeter-wave/THz communication systems.

Dr. Zhang was a recipient of the IEEE Antennas and Propagation Society (AP-S) Fellowship in 2023 and the URSI Young Scientist Award in 2024.

Mar Francis de Guzman (Member, IEEE) received the B.S. degree in electronics and communications engineering and the M.S. degree in electrical engineering from the University of the Philippines Diliman, Quezon City, Philippines, in 2015 and 2017, respectively. He is currently pursuing the D.Sc. degree in technology with the Aalto University School of Electrical Engineering, Espoo, Finland.

In 2023, he was a Visiting Doctoral Student with the Centre for Wireless Communications, University of Oulu, Oulu, Finland. His research interests include radio channel measurements, simulations, and modeling for 6G wireless communication systems.

Yejian Lyu received the bachelor's and master's degrees from Tongji University, Shanghai, China, in 2017 and 2020, respectively, and the Ph.D. degree from Aalborg University, Aalborg, Denmark, in 2024.

He is currently a Post-Doctoral Researcher with the Terahertz Wireless Communications Laboratory, Shanghai Jiao Tong University, Shanghai. His research interests include radio channel sounding and modeling for 6G communications and THz applications, such as THz integrated sensing and communication.

Katsuyuki Haneda (Member, IEEE) is currently an Associate Professor with the Aalto University School of Electrical Engineering, Espoo, Finland. He has authored and co-authored a number of best paper and student paper awards at the IEEE Vehicular Technology Conference and the European Conference on Antennas and Propagation, among others. He was the Co-Chair of a disciplinary working group on radio channels in European COST Actions CA15104 Inclusive Radio Communication Networks for 5G and Beyond (IRACON) between 2016 and 2020. His current research interests include high-frequency radios, such as millimeter-wave and beyond, and wireless for medical and smart-city applications.

Dr. Haneda also received the R. W. P. King Paper Award from the IEEE TRANSACTIONS ON ANTENNAS AND PROPAGATION in 2021, together with Dr. Usman Virk. He was the Technical Program Committee Co-Chair of the 17th European Conference on Antennas and Propagation (EuCAP 2023), Florence, Italy. He was an Associate Editor of the IEEE TRANSACTIONS ON ANTENNAS AND PROPAGATION and an Editor of the IEEE TRANSACTIONS ON WIRELESS COMMUNICATIONS between 2013 and 2018. He was a Guest Editor of special issues on Antennas and Propagation Aspects of In-Band Full-Duplex Applications and Artificial Intelligence in Radio Propagation for Communications in the IEEE TRANSACTIONS ON ANTENNAS AND PROPAGATION in 2021 and 2022, respectively. He is also a Guest Editor of the upcoming Special Section on Sub-THz and THz Radio Propagation: Measurements and Characterization in the IEEE OPEN JOURNAL OF ANTENNAS AND PROPAGATION.

Nuutti Tervo (Member, IEEE) received the B.Sc. (Tech.), M.Sc. (Tech.), and D.Sc. (Tech.) degrees (Hons.) from the University of Oulu, Oulu, Finland, in 2014, 2014, and 2022, respectively.

He is currently an Assistant Professor (tenure track) with the Centre for Wireless Communications-Radio Technologies (CWC-RT) Research Unit, University of Oulu. From April 2022 to March 2024, he was a Post-Doctoral Researcher with the University of Oulu, where he led the RF signal processing research at the RF group. Since September 2023, he has been a coordinator of the Devices and Circuit Technologies research area in the 6G Flagship program by the Academy of Finland. In October 2023 he received the title of Docent in RF transceiver signal processing from the University of Oulu. From October to November 2023, he was a Visiting Scholar with the Excellence Center at Linköping-Lund in Information Technology (ELLIIT) focus period at Lund University, Lund, Sweden. He has a strong background in different fields of wireless communications, including RF transceivers, radio channel modeling, signal processing, and system-level analysis. Around those topics, he has authored or co-authored more than 70 international journal and conference articles and he holds patents.

Dr. Tervo was a recipient of the Young Scientist Award of the URSI XXXV Finnish Convention on Radio Science, Tampere, in 2019. In 2020, he co-authored a paper that received the 50th EuMC Microwave Prize 2020, Utrecht, The Netherlands.

Aarno Pärssinen (Senior Member, IEEE) received the M.Sc. degree (Licentiate) in technology and the D.Sc. degrees in electrical engineering from the Helsinki University of Technology, Espoo, Finland, in 1995, 1997, and 2000, respectively.

From 1994 to 2000, he was with the Electronic Circuit Design Laboratory, Helsinki University of Technology, where he was involved in direct conversion receivers and subsampling mixers for wireless communications. In 1996, he was a Research Visitor with the University of California at Santa Barbara, Santa Barbara, CA, USA. From 2000 to 2011, he was with the Nokia Research Center, Helsinki, Finland. From 2009 to 2011, he served as a member of the Nokia CEO Technology Council. From 2011 to 2013, he was with Renesas Mobile Corporation, Helsinki, where he was a Distinguished Researcher and an RF Research Manager. From October 2013 to September 2014, he was an Associate Technical Director with Broadcom, Helsinki. Since September 2014, he has been with the Centre for Wireless Communications, University of Oulu, Oulu, Finland, where he is currently a Professor. He also leads the devices and circuits research area in the 6G flagship program financed by the Academy of Finland. He is also one of the original contributors to Bluetooth low energy extension, now called BT LE. He has authored and co-authored one book, two book chapters, more than 200 international journal and conference articles, and holds several patents. His research interests include wireless systems and transceiver architectures for wireless communications with a special emphasis on RF and analog integrated circuits and system designs.

Dr. Pärssinen served as a Solid-State Circuits Society representative for the IEEE 5G initiative from 2015 to 2019. He has been a member of the Technical Program Committee of the IEEE RFIC Symposium and the ESSERC European Solid-State Electronics Research Conference (ESSERC) since 2024. He was a recipient of the European Microwave Prize on the Best Paper at the European Microwave Conference 2020. He served as a member of the Technical Program Committee of the International Solid-State Circuits Conference from 2007 to 2017, where he was the Chair of the European Regional Committee from 2012 to 2013 and the Wireless Subcommittee from 2014 to 2017.

Pekka Kyösti received the M.Sc. degree in mathematics and the D.Sc. degree (Hons.) in communications engineering from the University of Oulu, Oulu, Finland, in 2000 and 2018, respectively.

From 2008 to 2012, he was actively involved in developing methods for multiple-input multiple-output over-the-air testing. From 1998 to 2002, he was with Nokia Networks, Helsinki, Finland, and from 2002 to 2016, he was with Elektrobit/Anite, Oulu. Since 2016, he has been a Part Timer with Keysight Technologies Finland Oy, Oulu. Since 2002, he has been involved in radio channel measurements, estimation, and modeling. He is currently the Research Director of the 6G Flagship Programme and a Docent (Adjunct Professor) with the Centre for Wireless Communications (CWC), University of Oulu, and a Senior Specialist with Keysight Technologies Finland Oy. He has acted as a Contributor and the Task Leader roles in many past research projects, such as Wireless World Initiative New Radio (WINNER) (I, II, +) and Mobile and wireless communications Enablers for the Twenty-twenty Information Society (MEITS). He has also contributed to channel modeling on many standardization forms, such as International Telecommunication Union - Radio technology (ITU-R), 3GPP (RAN1 and RAN4), CTIA, and IEEE 802. His current research interests include radio channel characterization for 6G systems, and channel modeling and over-the-air emulation for 5G systems.

Dr. Kyösti has been a Guest Editor in special issues of *IET Microwaves, Antennas & Propagation*, the IEEE JOURNAL ON SELECTED AREAS IN COMMUNICATIONS, IEEE ACCESS, the IEEE OPEN JOURNAL OF ANTENNAS AND PROPAGATION, and the IEEE TRANSACTIONS ON ANTENNAS AND PROPAGATION, in years 2019–2024.